Supplementary Information
From Slater to Mott physics by epitaxially engineering electronic correlations in oxide interfaces

C. Lupo*, E. Sheridan*, E. Fertitta, D. Dubbink, C. J. Pickard, C. Weber

May 18, 2021

S1 Supplementary Discussion

Magnetic and electronic insights of the unstrained $LaTiO_3/LaFeO_3$ heterostructure

Different initial magnetic conditions and outcomes

In our calculations we considered four different initial magnetic conditions as shown in Fig S1. The G-type I ordering (Fig S1a) represents the configuration with non magnetic Ti ions and antiferromagnetic Fe with in plane Néel ordering. The G-type II ordering, shown Fig S1c, corresponds to the magnetic ordering of both bulk $LaTiO_3$ and $LaFeO_3$ where the interaction between nearest neighbours transition metal is antiferromagnetic both in plane and out of plane.
As shown by the density of states, a different electronic configuration is stabilised according to the initial fixed magnetic pattern. In particular if a non-magnetic condition is initially set (Fig S1b), in the obtained relaxed $LaTiO_3/LaFeO_3$ heterostructure we individuate charge transfer from Ti to Fe, with the Fe ions optimised in a 2+ low spin state.
If the initial configuration is G-type I, the relaxed electronic/magnetic configuration still shows that the Ti/Fe charge transfer mechanism occurs but with Fe being in a 2+ high spin configuration. In particular the continuous and dashed blue line shown in the density of states, outline that the interaction between the two Fe_1 and Fe_2 ions is antiferromagnetic. As already stated in the main text, for each Fe ions, the electron transferred from Ti ($3d$) to Fe ($3d$ forms a localized Fe t_{2g} singlet at the top of the valence band. Interestingly if the initial magnetic order is G-type II (see Fig S1c), the charge transfer is quenched and the band picture of the $LaTiO_3/LaFeO_3$ heterostructure bears similarities with the bulk $LaTiO_3$ and $LaFeO_3$ counterparts. Indeed we can notice that the ($3d$) bands of Fe^{3+} (Ti3+) are localised below (above) the O ($2p$) bands, as in the bulk $LaFeO_3$ ($LaTiO_3$) counterpart. Differently from cases in S1a and S1b, the lower conduction band is mainly characterised by the empty spin channel of the Fe ($3d$) bands.
In the case where an initial ferromagnetic condition (for the Fe ion) is set, with Ti being non magnetic, the density of states obtained in Fig S1d) outlines a solution with charge transfer from Ti to Fe being the Fe_1 and Fe_2 ions in ferromagnetic order.

We clarify that the ground state of the system is represented by the case with charge transfer and Fe^{2+} in high spin configuration S1a, while the other three outcomes represent metastable states at higher energies.

Orbital and atomic resolved density of states of the ground state configuration

In Fig. S2 we present the total and orbital resolved density of states for the $LaTiO_3/LaFeO_3$ superlattice. In particular, we separate the data into three separate panels so as to disentangle the role of the constituent components of the superlattice. In Fig. S2a we see the broad manifold of oxygen states that extend from the Fermi level, where they are primarily hybridised with the d-states of iron, to -7 eV where again there is a significant hybridisation with the states within the iron manifold. Fig. S2b serves to illustrate the empty Ti d-states that locate 2eV above the Fermi level, and are a superposition of t_{2g} and e_g states. Upon forming the interface, the nominal Ti^{3+} transfers its charge away pushing the Ti-d t_{2g} states 2 eV above the Fermi level, instead of below it. The full electron manifold of the antiferromagnetic Fe states is shown in Fig S2c, where the specific Fe_1 and Fe_2 states are illustrated in Fig S1c. As mentioned in the main text, we observe spin blocking at the Fermi level where the transferred t_{2g} electron localises at the valence band maximum, with opposite spin orientations for the antiferromagnetic pairs. The sizeable hybridisation with the oxygen states in this region is indicative toward a super-exchange coupling between these magnetic states. Moreover, we remark that the Fe-manifold inherits the main features of its parent compound $LaFeO_3$, with a d-band splitting above and below the oxygen manifold. To merge the Fe-manifold into itself and destroy this splitting necessitates the full band to move above the oxygen band, as is observed for the non magnetic scenario in Fig. S1b. In this case, the energy penalty to destroy the AFM state hints toward the stabilisation of robust AFM ground state.

A-site polar distortion: La and Y cases

We have enphasised so far that the ground state of the heterostructure is characterised by charge transfer from Ti to Fe with Fe in 2+ high spin configuration and with protected antiferromagnetic interactions between the Fe ions in the FeO2 layer. A similar result is obtained in previous work where $YTiO_3/YFeO_3$ [16] was considered. We note that in the latter work the A-site (Y instead of La) ion has a smaller ionic radius (respectively 104 and 117.2 pm [15]). Since the electronic properties are very similar to the materials studied in our work, we conclude that the ionic radius of the A-site ion is not key to the super-exchange process. Additionally, a feature that we observed in the La based heterostrucure is an anti-polar distortion of the La toward the FeO_2 layer. As shown in Fig S3a, in absence of charge transfer, the oxide layers are isopolar (with total nominal charge ± 1) and the La is aligned in its oxide plane (LaO). However, when the charge transfer occurs from Ti to Fe, an internal electric field is created, giving rise to an imbalance of charge between the layers. To screen this effect, an antiferroelectric distortion of the La ion of 0.2 Åoccurs and it prevents further electron transfer by balancing the difference in electrochemical potential between Fe and Ti through aligning their constituent oxygen bands. We confirm that for $YTiO_3/YFeO_3$ the antiferroelectric distortion of the Y ion is enhanced to 0.25 Å, as expected since the Y ion is lighter than La.

Role of U

The crucial mechanism uncovered in our analysis is the charge transfer between Ti and Fe. In our calculation we set the values of U based on previous studies of the $LaTiO_3/LaFeO_3$ interface [9]. In particular $U_{eff}(Fe) = 4.8eV$ and $U_{eff}(Ti) = 3eV$. In Fig.1d of the main manuscript we show a rich phase diagram, where we reported the ground state of the heterostructure and its low-lying metastable states. The small energy differences between the optimised configurations indicate a possible sensitivity of results on different choices of the U. In particular, when considering the energy difference between the CT and NO CT case, we should notice that the effective interaction of $Fe^{2}+$ (d^6) HS state is $U - 3J$, in contrast to $U + 4J$ in the HS state of Fe^{3+}(d^5) [6]. To get further insights in this regard, we extended our analysis to key values of U. In Fig.S4 we show the energy dependence of the two configurations of $LaTiO_3/LaFeO_3$ interface in interest, while are charge-transfer high-spin (CT HS, with Fe^{2+}_{HS} and Ti^{4+}) and no charge-transfer (NO CT, with Fe^{3+}_{HS} and Ti^{3+}) configurations, as a function of different values of $U_{eff}(Fe)$. Each data point represents a fully relaxed $LaTiO_3/LaFeO_3$ heterostructure with fixed $U_{eff}(Ti) = 3eV$ and initial magnetic conditions G-type I and G-type II as defined in Fig.**??**.
We notice that the CT HS is confirmed to be the ground state of the heterostructure. In particular, for a fixed U, U_{eff} will be smaller for the CT HS and larger for the NO CT. Therefore the energy difference between the two configurations will further increase because of the Hund's J interaction. For example, if we consider $U(Fe) = 5$ eV and $J = 0.5$ eV, the effective U for Fe^{3+}_{HS} would be $U_{eff} = U + 4J = 7$eV while for Fe^{2+}_{HS} we consider $U_{eff} = U - 3J = 3.5$ eV (respectively indicated by the gray symbols). From our results shown in Fig. S4, we can estimate that the energy difference is ≈ 1.5 eV, therefore the CT HS is the most stable one.

Epitaxial engineering of many-body correlation strenght: multisubstrate analysis

Mott to Slater transition: engineering of itinerant magnetism with compressive strain

In this section we extend in more details the results showed in Fig 1c and 2 of the main text. In Fig S5 we report the density of states obtained considering different substrates in their stabilised ground state configuration: charge transfer from Ti to Fe, with $Fe^{2}+$ in high state state.
For each density of state, the two Fe ions in the unit cell are shown with continuous and dashed blue line, highlighting that the long range antiferromagnetic is protected against potential epitaxially engineered magnetic phase transitions.
A closer look at the Fe d states, allows to distinguish different features as increasing in-plane strain is applied.
We start considering the substrate with the biggest lattice constant ($LaLuO_3$). In this case we identify a localised character of the filled Fe-d above the O$-p$. This picture changes as we select a substrate with a smaller lattice constant. In particular with increasing in-plane compressive strain, we can individuate a progressive broadening of the d bands concomitant to an enhanced hybridisation with the oxygen bands, giving rise to an itinerant magnetic behaviour of the Fe ion, typical of Slater insulators.

Ferromagnetic solutions: Metal-to-insulator transition

Using spin-assisted random structure searching we can explore the phase space around the energy minimum and what intermediate spin-states are accessible. We use the AIRSS package [11, 12] interfaced with Quantum Espresso to execute the search. The overall procedure has two primary constraints: (i) the starting spin configuration and (ii) fixed in-plane lattice parameters. As such, the workflow amounts to choosing starting configuration which is then relaxed subject to fixed in-plane parameter from which a ground state configuration is found. In Fig. 1b we show the energetic distribution of total magnetisation per cell clamped to the LAO substrate. What emerges from the search is a classification of the possible spin-states into four categories, in order of likelihood. The most likely candidates found have an antiferromagnetic ordering, occurring in 74% of cases and are followed by the ferromagnetic structures, which occur in 21% of instances. In the remaining cases, which comprise of only 5%, are the systems in which there is an overall spin- and charge-disproportion, although there are remnants signatures of an overall magnetic order, depending on the magnitude of the total magnetisation. We note that for these calculations a coarse k-mesh is used, and so the energies should only be trusted qualitatively. We have confirmed that by taking representative candidates from the search that the energy difference between the ground state and predicted antiferromagnetic states is less than 0.001 meV, as expected. The ferromagnetic states lie between 10-100 meV above the ground state. There are some ferromagnetic and antiferromagnetic states that are 100-500 meV above the ground state, and these have unequal magnetic moments on their magnetic ions, and thus exhibit features characteristic of a spin density wave. Finally, the states with spin and charge disproportion are found to lie close to 1 eV above the antiferromagnetic ground state. The spin-assisted random structure search highlights the importance of the low-lying ferromagnetic configurations, being the most likely metastable state for $LaTiO_3/LaFeO_3$ with a different magnetic order. To this end, we investigate the behaviour of the energy difference between the ferromagnetic and antiferromagnetic configurations for the collection of substrates examined in the main part of the text.

By extending the spin assisted magnetic structure search beyond $LaAlO_3$ we identify an active polar mode in the titanium octahedral, resulting in a significant change to the local Ti environment. In Fig S6a we present all possible energetically favourable local geometries predicted by the structure search. Upon entering the Mott phase there is a significant Ti-polarisation that lowers the energy of charge disproportioned metastable states, as illustrated with the discovery of a number of different low-lying magneto-structural phases. In the opposite limit on the $LaAlO_3$ substrate the octahedral complex is always stable. Moreover, in Fig S6b we present the variation of the band gap across the range of substrates studied. The orbital reconstruction of the Ti-d states at the conduction band minimum due to a tetrahedrally coordinated environment shifts the relative energy between the Fe-d states at the valence band minimum. Thus, the increase of the band gap in the Mott phase has a cooperative electro-structural origin.

Structural optimization of the Slater and Mott insulators

Slater systems under high compressive strain We already emphasized in the main text the volume expansion of the Slater systems. In Fig S7 we provide further insights about it and in particular, the E-V plot, shows that the $LuAlO_3$and $YAlO_3$ configurations belong

to a different parabola in the landscape of the potential energy surface. We also compare the electronic configurations and the energies of the relaxed structure with the ones constrained on an extrapolated volume. We notice that the latter are at a higher energy than the former and are characterised by insulating behaviour with reduced band gap and localised character of Fe ($3d$) states. A closer comparison between density of states of the relaxed configurations and the structure constrained to the extrapolated volume (see Fig S7), reveals at last that volume expansion together with increasing of octahedral rotations (see Fig. S8c), favour the lowest energy configurations for $LaTiO_3/LaFeO_3$ constrained on $LuAlO_3$and $YAlO_3$. Moreover, we note that an expansion of the c-axis is concomitant with a broadening of the peak of the e_g orbital and increasing hybridisation with the oxygens p bands, giving rise to an itinerant magnetic behaviour of the Fe ion, typical of Slater insulators. We note that the volume expansion is only obtained in the magnetic Slater insulator, whereas the non magnetic counterpart is not going through a similar process. Indeed the Slater system provides a mechanism to optimise its kinetic energy, with an associated increase of the La antiferroelectric polarization (see Fig S8b).

Since the in-plane parameters are fixed to the given substrates, the volume expansion is associated with the increasing of the c-lattice parameter which might suggest that the obtained structures are not stable perovskites. To asses the geometric stability and distorsion of the crystal structure in analysis, we propose an extended definition of the Goldscmidth tolerance factor (t) [7]. The t is primarily defined for ABX_3 pervoskites, considering the ratios of the constituent ionic radii A, B, X as $t = (R_A + R_X)/\sqrt{2}(R_B + R_X)$. In case of $LaTiO_3/LaFeO_3$ interface, we used a more generalised definition the tolerance factor previously introduced in Ref.[5] and defined for $A_2BB'O_6$ double perovskites as $t = 2 * (R_A + R_X)/\sqrt{2}(R_B + R_{B'} + 2 * R_X)$. Note that the radii for La, Fe and Ti are obtained from the optimised structures while the ionic radius of O^{2-} is fixed to 126 pm [15]. In case of an ideal perovskite ABC_3 with a cubic closed packed structure the value of the Goldschmidt factor is $t = 1$ (e.g $SrTiO_3$). The more t deviates from 1 ($t < 1$), the lower the symmetry of the stabilised structure is, up to an optimal lower bound for perovskite formability. On this regard, our result (see Fig S8a) shows that the volume expansion, which occurs in case of clamping the $LaTiO_3/LaFeO_3$ on $YAlO_3$ and $LuAlO_3$substrates, is concomitant with a decreasing of the t ratio and hence a further reduction of the symmetry (due to increased octahedral distortions as in Fig. S8c) of the structure, albeit within the stability range of the perovskites.

Thus we have observed so far that the Slater systems use collaborative mechanism between magnetism and structural deformation (volume expansion, increased octahedral rotation, enhanced La polarization) to lower the energy and stabilises an itinerant magnet.

Mott systems under high tensile strain In fig S8(b), we study the behaviour of the angle γ defined by Ti and its apical oxygens, and observe that it is constant to π up to $SrTiO_3$. Thus for all the substrates with $a < 3.905$, the Ti is in its centrosymmentric position. When the system is clamped on substrates with lattice parameters greater than 4 Å, the optimised superlattice is characterized by a non centro-symmetric position of the Ti inside its oxygen cage.

Temperature dependence of the high spin state

Calculation details We perform One Shot (OS) DFT+DMFT calculations at $T = 290K = 1/40$ eV. The low-energy tight-binding hamiltonian is constructed in the basis of maximally localised Wannier Functions (MLWFs) using the Wannier90 code[13]. The DMFT self-consistency cycle is implemented using the TRIQS/DFTTools libraries[1]. For different symmetry inequivalent correlated sites the effective impurity problem is solved using the continuous-time Quantum Monte Carlo hybridisation-expansion solver as implemented in TRIQS/CTHYB[14]. In this scenario, we can restrict the correlated subspace to that of the Fe_1 as a result of the symmetry equivalence at the paramagnetic DFT-level. The double counting correction of Held[8] is applied to the correlated subspace as the local interacting Hamiltonian is expressed in the Slater-Kanamori form including spin-flip and pair-hopping processes. The Hubbard U parameter for the Fe_1 site is $U = 5.3$ eV and the Hund's coupling parameter is set to $J = 0.5$ eV, to match the value of the effective Hubbard parameter as used in the magnetic DFT+U calculations. To reduce noise originating from the Monte Carlo statistics we sample the Legendre coefficients G_l directly within the TRIQS/CTHYB solver. The full frequency spectral function $A(\omega)$ is obtained via analytically continuing the Matsubara Green's function using The TRIQS/MaxEnt library[10]. All results are performed within the "one-shot" DFT+DMFT approximation and neglect the effect of charge self-consistency. The starting configuration used to generate the low energy effective Hamiltonian is a paramagnetic DFT calculation without Hubbard U correction where the seed structure is a converged LSDA+U calculation on the $LaLuO_3$ substrate.

The effect of temperature In Fig. S9(a) we illustrate that the magnetic Fe^{2+} state is recovered at room temperature within the paramagnetic DMFT approximation and predicts the same orbital ordering as the magnetic DFT prediction. We also emphasise in Fig. S9(a) that paramagnetic DFT is only capable of obtaining a low-spin non-magnetic configuration, with fully occupied t_{2g} levels. Moreover, in Fig. S9(b) we show the converged imaginary part of local interacting orbital resolved matsubara Green's function, $\Im mG(i\omega_n)$, which attains an insulating-like character at zero frequency. Similarly, the imaginary component of the converged impurity orbital resolved self energy $\Im m\Sigma(i\omega_n)$ is presented in Fig. S9(c) and shows a clear distinction between the build-up of interactions within the strongly correlated Fe-d impurity states. Notably, the fully-occupied d_{yz} has as significantly flatter self-energy than its counterparts, as should be expected in an almost full orbital[4], while the additional orbitals all attain a negligble quasiparticle weight, as an indication of their localised character. The retention of the orbital reordering of the Fe^{2+} state at $T = 290K$ within the DMFT approximation demonstrates that many-body correlations persist and can mediate long-range magnetic order beyond the zero temperature approximation of magnetic DFT+U.

To assess the dependence of magnetic moment of Fe at room temperature we directly sample the fluctuating paramagnetic moment $S = \sqrt{\langle S_z^2 \rangle}$ where $S_z = \frac{1}{2}\sum_\mu (n_\uparrow^\mu - n_\downarrow^\mu)$ is the total z-component of the isotropic magnetic moment summed over the Fe-d orbitals. From this, we estimate that the local magnetic moment at room temperature is approximately $m_{Fe}^{DMFT} = 2.82\mu_B$. For zero temperature magnetic DFT we estimate that the magnetic moment of the high spin Fe to be $m_{Fe}^{DFT} = 3.46\mu_B$. Thus, we see that there is an overall reduction of the magnetic moment by 18% at room temperature due to thermal and quantum

fluctutations. Since the DMFT calculation treats the the fully rotational invariant vertex with the non-diagonal terms of the Hund's coupling (whereas in DFT only the diagonal terms are included), we also anticipate there is a reduction of the magnetic moment due to additional scattering terms, neglected in the vanilla DFT.

Through analytical continuation of the converged $G(\tau)$ using the maximum entropy technique the spectral function is obtained at $T = 290K$, as illustrated in Fig. S10 decomposed along the crystal field axes. We also provide a comparison to the $T = 0K$ scenario obtained with magnetic DFT+U clamped to the $LaLuO_3$ substrate. It is also observed in the spectral function that the Fe^{2+} paramagnetic state remains stable at higher temperatures and sustains the orbital ordering predicted by zero temperature magnetic DFT+U. However, we note that there is significantly less splitting between the upper and lower Fe-d valence bands within the DMFT approximation. As already discussed in relation to the magnetic moment, we attribute this to the dynamical spin effects captured by the Slater-Kanamori Hamiltonian. In addition, we remark that the maximally localised wannier functions are obtained only in the window of energy of the Fe-d manifold subsapce, and we neglect the contributions arising from the O-p states. As such, this will have an additional effect on suppressing the overall splitting of the Fe-d states[2, 3], due to the absence of O-p alignment across the interface in the Wannier basis. Moreover, we see that the Fe-d gap persists up to room temperature, indicative of room temperature Mott stabilisation of the magnetic insulator.

$(LaTiO_3)_2/(LaFeO_3)_2$ heterostructure

We extended our calculation to larger supercells. In particular we considered the $(LaTiO3)_2/(LaFeO3)_2$ heterostructure as shown in Fig.S11. Following the same procedures as for the (1/1) heterostructure, we optimised different configurations starting from a non-magnetic and a G-type II initial magnetic ordering. The density of states shows that, irrespective of the initial conditions, a charge transfer from Ti to Fe occurs, stabilizing Ti^{4+} and Fe^{2+}. Indeed the Ti d states characterise the conduction bands in the proximity of the Fermi level. On the other hand, the Fe-d states characterise the top of the valence bands, assuming a different character according to the stabilised spin state of the Fe^{2+}. Indeed in panel b) we identify a low spin state of both Fe1 ad Fe2, with filled t_2g states, while in panel c) the lifted symmetry of Fe1 and Fe2 indicate their antiferromagnetic interaction and for each Fe ions, we retrieve the characterization of the d manifold already observed in Fig 1c of the main text. We emphasise that also in the case of the 2/2 interface, the ground state is CT HS and the non-magnetic configuration is a metastable state higher in energy by ≈ 1.6 eV/f.u. Therefore, most of the observed features bear similarity with the (1/1) interface, although in this case, we can observe a reduced bandgap. Interestingly, a comparable result has been observed for the $YTiO_3/YFeO_3$ interface in Ref. [16] (Fig 2 in Ref.[16]), where the authors find that even if increasing the number of layers, charge transfer from Ti to Fe occurs, resulting in a high spin state for the Fe2+. Similarly to our case, the electronic properties of the 1/1 and 2/2 interface differ for the width of the d-d bandgap, which is reduced in the latter. Lastly, it is worth highlighting the structural deformation stemming from the cooperative charge-lattice degrees of freedom. Indeed, irrespective of the spin-state optimised, we observed the La anti-polar distortion triggered by the charge transfer from Ti layers to Fe layers. This

effect becomes even more interesting for this larger heterostructure. We can differentiate both aligned and misaligned LaO layers. In particular, La is aligned with its oxygen plane if in between a symmetric potential, as observed for the LaO layers in between the double $LaTiO_3$ or $LaTiO_3$. Instead, if the LaO is at the centre of asymmetric potential, the La ions move toward the more negatively charged layer, which in this case is represented by FeO_2.

S2 Supplementary References

References

[1] M. Aichhorn, L. Pourovskii, P. Seth, V. Vildosola, M. Zingl, O. E. Peil, X. Deng, J. Mravlje, G. J. Kraberger, C. Martins, M. Ferrero, and O. Parcollet. Triqs/dfttools: A triqs application for ab initio calculations of correlated materials. *Computer Physics Communications*, 204:200–208, 2016.

[2] S. Beck and C. Ederer. Charge transfer in $lavo_3$/$latio_3$ multilayers: Strain-controlled dimensionality of interface metallicity between two mott insulators. *Phys. Rev. Materials*, 3:095001, Sep 2019.

[3] H. Chen and A. Millis. Charge transfer driven emergent phenomena in oxide heterostructures. *Journal of Physics: Condensed Matter*, 29(24):243001, may 2017.

[4] C. M. de' Medici L. Modeling many-body physics with slave-spin mean-field: Mott and hund's physics in fe-superconductors. *In: Mancini F., Citro R. (eds) The Iron Pnictide Superconductors. Springer Series in Solid-State Sciences, vol 186*, 2017.

[5] M. R. Filip and F. Giustino. The geometric blueprint of perovskites. *Proceedings of the National Academy of Sciences*, 115(21):5397–5402, 2018.

[6] A. Georges, L. d. Medici, and J. Mravlje. Strong correlations from hund's coupling. *Annual Review of Condensed Matter Physics*, 4(1):137–178, 2013.

[7] V. M. Goldschmidt. Die Gesetze der Krystallochemie. *Naturwissenschaften*, 14(21):477–485, May 1926.

[8] K. Held. Electronic structure calculations using dynamical mean field theory. *Advances in Physics*, 56(6):829–926, 2007.

[9] J. E. Kleibeuker, Z. Zhong, H. Nishikawa, J. Gabel, A. Müller, F. Pfaff, M. Sing, K. Held, R. Claessen, G. Koster, and G. Rijnders. Electronic reconstruction at the isopolar $latio_3$/$lafeo_3$ interface: An x-ray photoemission and density-functional theory study. *Phys. Rev. Lett.*, 113:237402, Dec 2014.

[10] G. J. Kraberger, R. Triebl, M. Zingl, and M. Aichhorn. Maximum entropy formalism for the analytic continuation of matrix-valued green's functions. *Phys. Rev. B*, 96:155128, Oct 2017.

[11] C. J. Pickard and R. J. Needs. High-pressure phases of silane. *Phys. Rev. Lett.*, 97:045504, Jul 2006.

[12] C. J. Pickard and R. J. Needs. Ab initiorandom structure searching. *Journal of Physics: Condensed Matter*, 23(5):053201, jan 2011.

[13] G. Pizzi, V. Vitale, R. Arita, S. Blügel, F. Freimuth, G. Géranton, M. Gibertini, D. Gresch, C. Johnson, T. Koretsune, J. Ibañez-Azpiroz, H. Lee, J.-M. Lihm, D. Marchand, A. Marrazzo, Y. Mokrousov, J. I. Mustafa, Y. Nohara, Y. Nomura, L. Paulatto, S. Poncé, T. Ponweiser, J. Qiao, F. Thöle, S. S. Tsirkin, M. Wierzbowska, N. Marzari, D. Vanderbilt, I. Souza, A. A. Mostofi, and J. R. Yates. Wannier90 as a community code: new features and applications. *Journal of Physics: Condensed Matter*, 32(16):165902, jan 2020.

[14] P. Seth, I. Krivenko, M. Ferrero, and O. Parcollet. Triqs/cthyb: A continuous-time quantum monte carlo hybridisation expansion solver for quantum impurity problems. *Computer Physics Communications*, 200:274–284, 2016.

[15] R. D. Shannon. Revised effective ionic radii and systematic studies of interatomic distances in halides and chalcogenides. *Acta Crystallographica Section A*, 32(5):751–767, Sep 1976.

[16] H. Zhang, Y. Weng, X. Yao, and S. Dong. Charge transfer and hybrid ferroelectricity in $(\mathrm{yfeo}_3)_n/(\mathrm{ytio}_3)_n$ magnetic superlattices. *Phys. Rev. B*, 91:195145, May 2015.

S3 Supplementary Figures

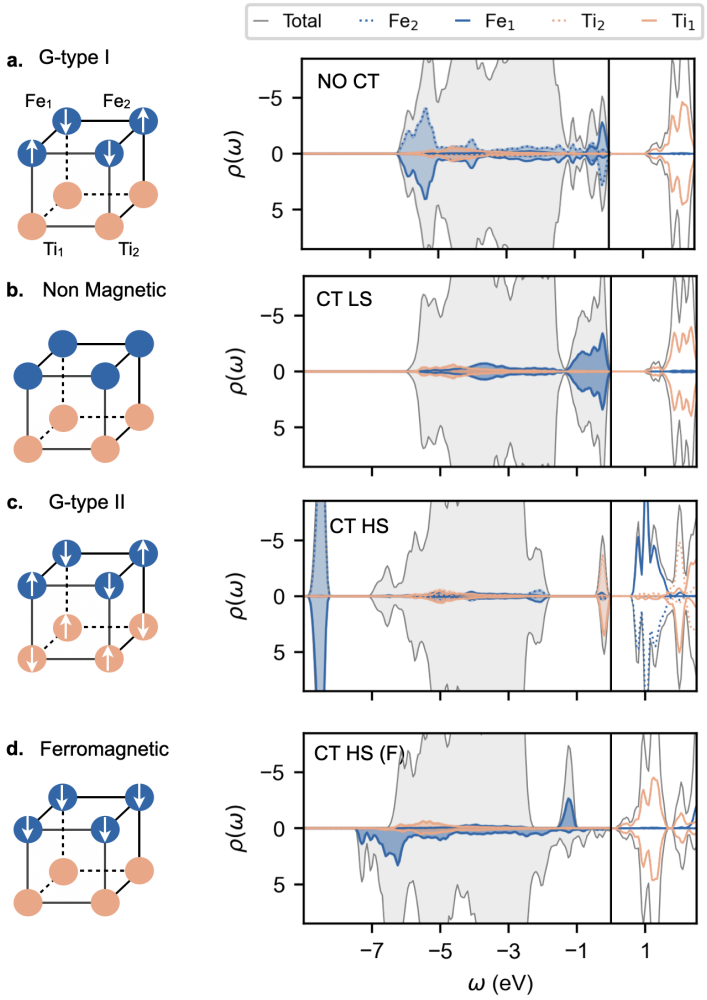

Figure S1: The total and species resolved density of states for (a) G-type I (b) Non-Magnetic, (c) G-type II antiferromagnetic and (d) ferromagnetic (only Fe ions) configurations of the $(LaTiO_3)_1/(LaFeO_3)_1$ superlattice. In every instance, the full Ti-d and Fe-d manifolds are shown and are decomposed into their $Fe_{1,2}$ or $Ti_{1,2}$ spatial labels.

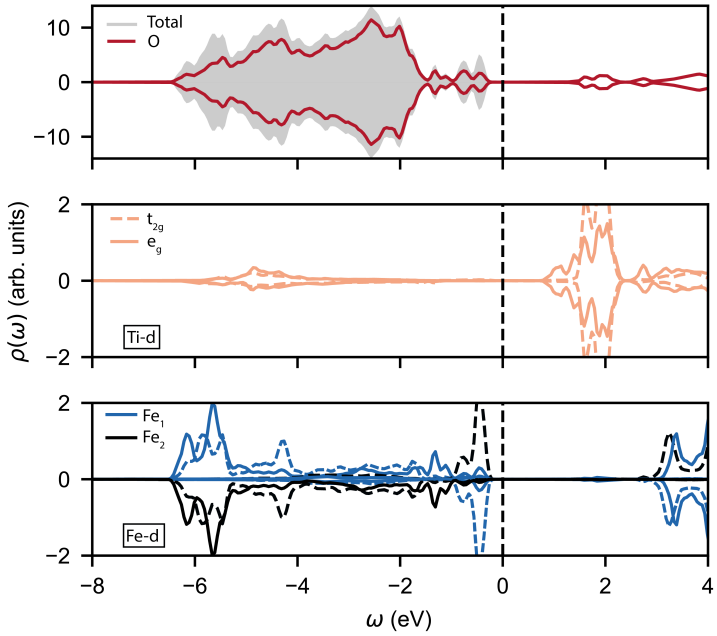

Figure S2: (a) The total and orbital resolved density of states for the O p majority (above axis) and minority (below axis) spin-species at the $(LaTiO_3)_1/(LaFeO_3)_1$ superlattice. (b) The orbital resolved density of states for the full Ti electronic manifold, decomposed into t_{2g} and e_g components. (c) The orbital resolved density of states for the full Fe electronic manifold, decomposed into t_{2g} and e_g components and distinguished by atomic label.

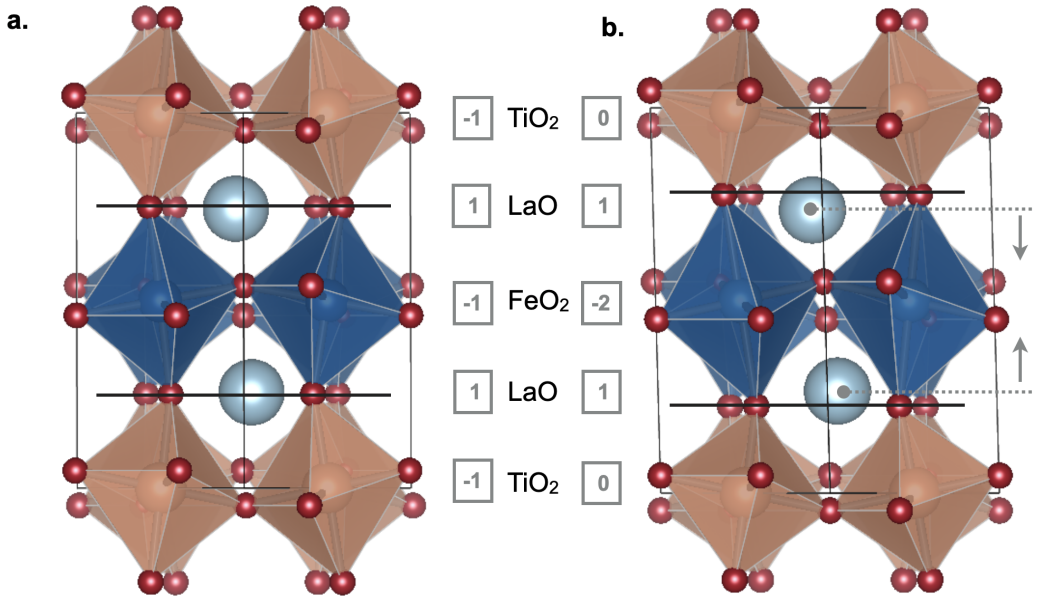

Figure S3: The $LaTiO_3/LaFeO_3$ heterostructure with electronic reconstuction at the interface (a) without charge transfer and (b) with charge transfer. For each case, we identify the nominal charge of the associated layers and the La-O displacement.

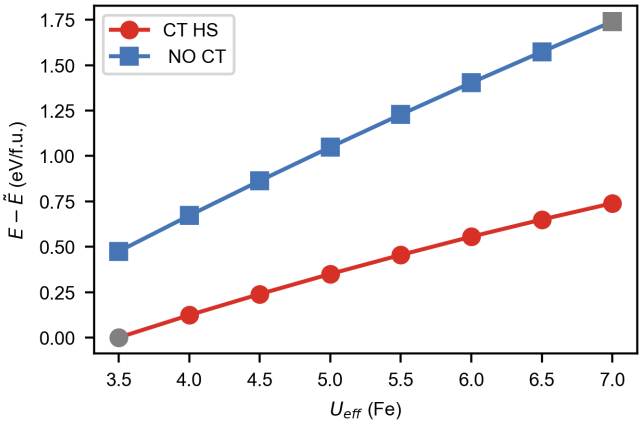

Figure S4: Energy dependence of the two configurations of the $LaTiO_3/LaFeO_3$ interface, which are charge-transfer high-spin (CT HS, with Fe^{2+}_{HS} and Ti^{4+}) and no charge-transfer (NO CT, with Fe^{3+}_{HS} and Ti^{3+}) configurations as a function of different values of effective Coulomb repulsion for Fe, while the value on Ti has been fixed to $U_{eff}(Ti) = 3eV$. For plotting purposes, the energies are rescaled with respect to $\tilde{E}$ which is the lowest energy found in the shown data set.

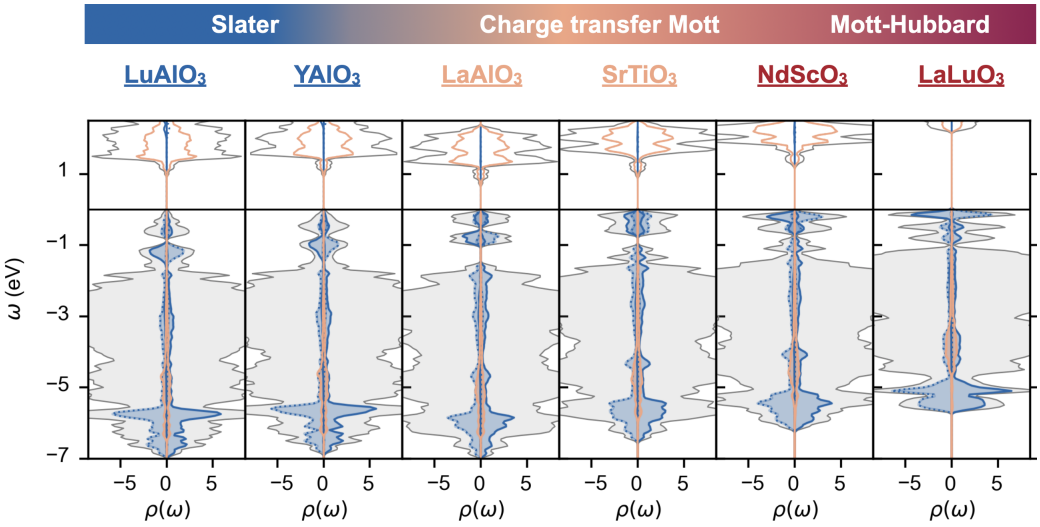

Figure S5: Density of states of the charge transfer high spin (CT HS) configuration across all the substrates considered in our work with the Fermi level being shifted to the top of the valence band.

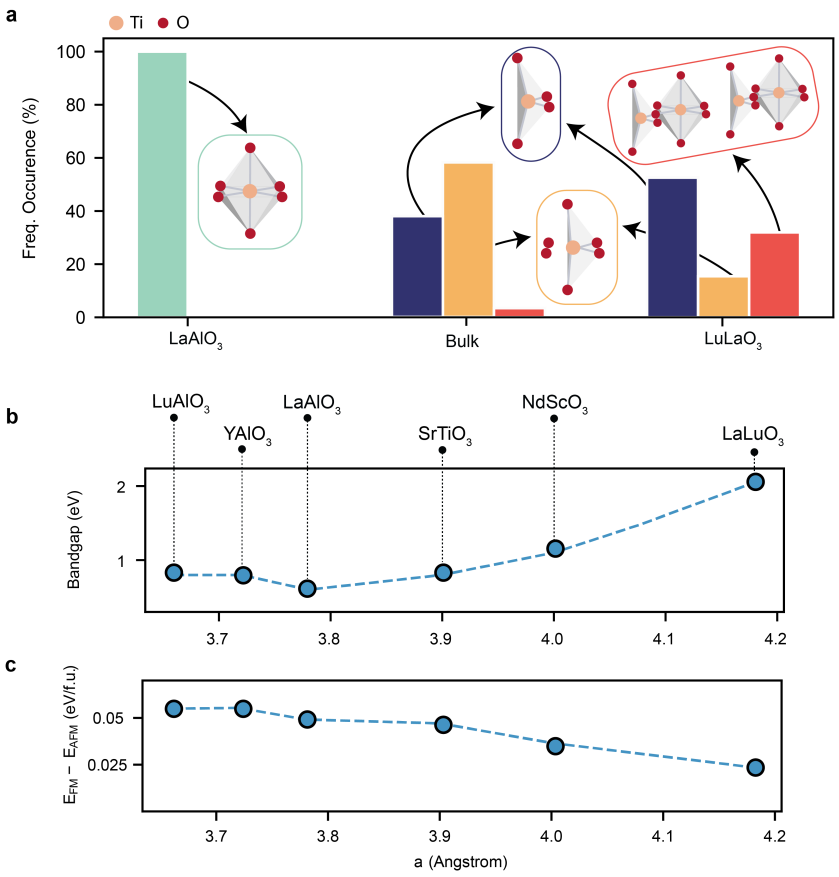

Figure S6: (a) The local O-Ti-O coordinated phase space predicted by by spin assisted ab-initio random structure searches across the Slater to Mott transition. For each histogram the energetic ordering goes from left to right. (b) The substrate dependent behaviour of the band-gap across series of substrates examined. (c) The difference between the ferromagnetic and G-type I antiferromagnetic configurations across the studied substrates.

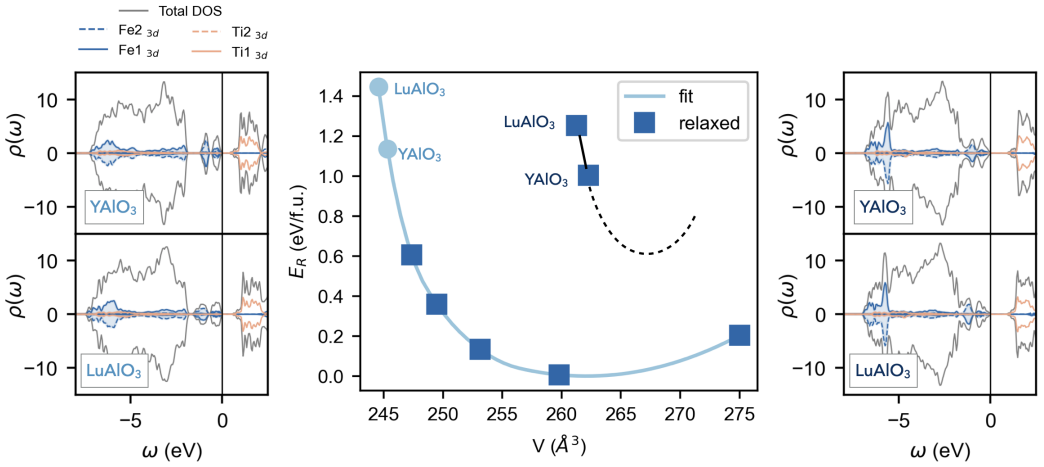

Figure S7: Energy differences of the relaxed volumes (squares) of the $LaTiO_3/LaFeO_3$ heterostructure with charge transfer from Ti^{4+} to Fe^{2+}_{HS} configuration for different selected substrates (labels), with respect to the bulk. For $LuAlO_3$and $YAlO_3$ substrates, fitted volumes are also shown (circles) with the associated density of states in the side panels. Indeed note that $LuAlO_3$and $YAlO_3$ do not follow the same equation of state as the other substrates. Thus, two energy/volume profiles are added as guide to the eyes corresponding to different character of the e_g orbitals, localised- Mott or itinerant-Slater, shown in the density of states (side panels). The comparison of the energy of the two systems between the extrapolated volumes (circles) and the relaxed ones (squares), reveals that there is a further energy reduction when $LuAlO_3$ and $YAlO_3$ expand their volume.

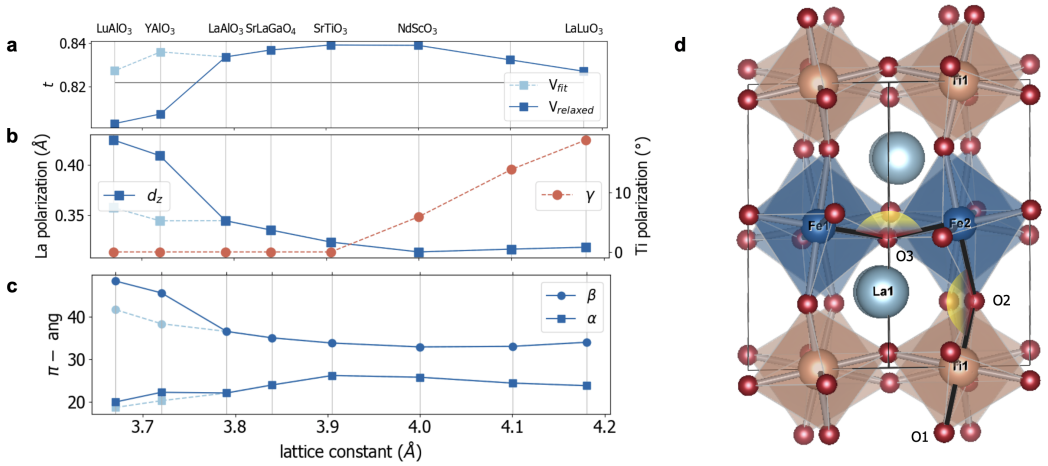

Figure S8: Analysis of the structural degrees of freedom for the $LaTiO_3/LaFeO_3$ heterostructure with charge transfer from Ti^{4+} to Fe^{2+}_{HS} (CT HS) configuration clamped on selected substrates (labels). In particular we show the behaviour of the Goldschmidt tolerance factor (a), the La (d_z)and Ti (γ) polarization (b) and the angles (c) as defined in the structure shown in panel (d). In particular: d_z is the offset along z direction of the La from the La_1O_2 plane, $\gamma = \pi - \widehat{O_2Ti_1O_1}$, $\beta = \widehat{Fe_1O_3Fe_2}$ and $\alpha = \widehat{Fe_2O_2Ti_1}$ For $LuAlO_3$and $YAlO_3$ substrates, the quantities in analysis are computed for the fitted volumes (light blue) along the dashed line shown in Fig. (2b) in the main text. The gray solid line in panel b refers to the tolerance factor computed considering the ionic radii from [15].

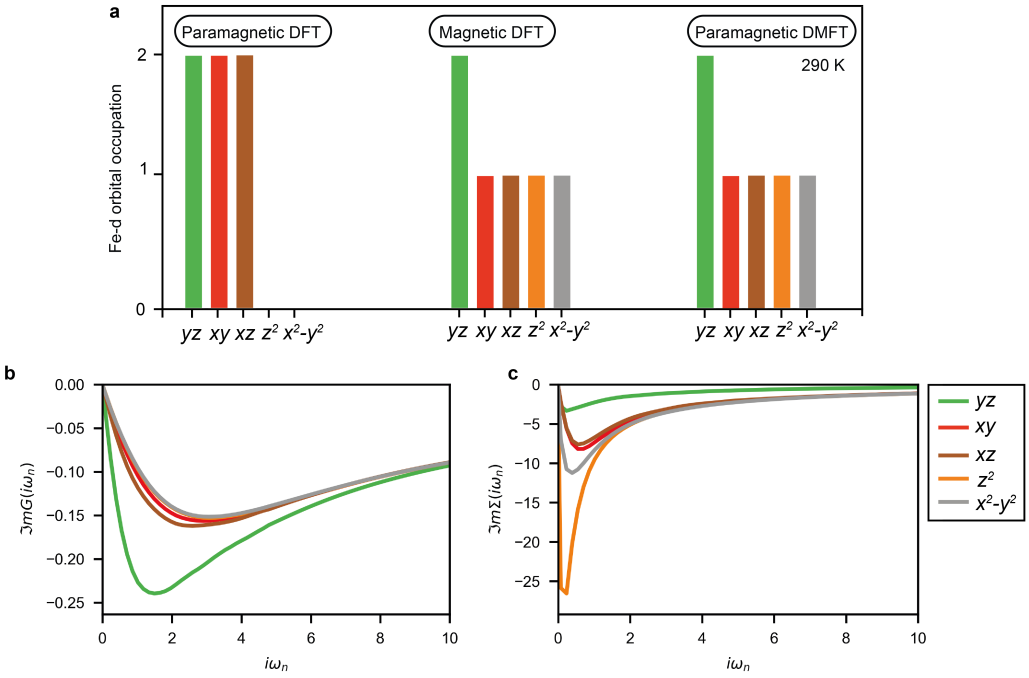

Figure S9: (a) Histogram for the Fe-d orbitally resolved occupations on the $LaLuO_3$ substrate as predicted by *(i)* paramagnetic DFT, *(ii)* magnetic DFT and *(iii)* paramagnetic DMFT at T=290 K (b) Orbitally resolved imaginary part of the impurity green's function $\Im mG(i\omega_n)$ and (c) imaginary part of the self energy $\Im m\Sigma(i\omega_n)$ predicted at T=290 K.

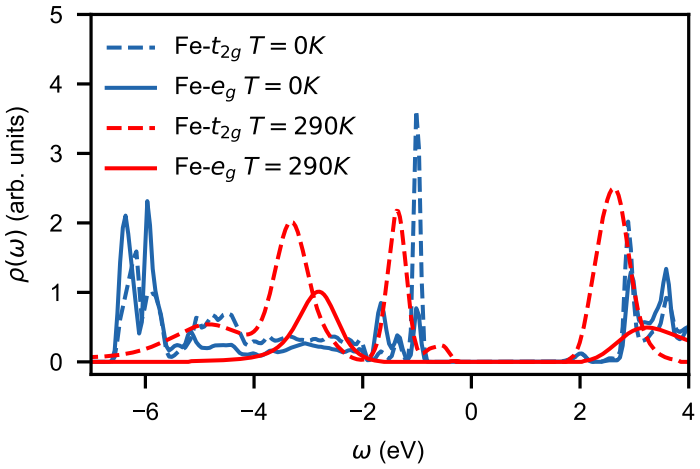

Figure S10: Orbitally resolved Fe-d spectral function on the $LaLuO_3$ substrate decomposed along the octahedral crystal field axes with absolute spin components at T=0K (magnetic DFT) and T=290K (paramagnetic DFT+DMFT).

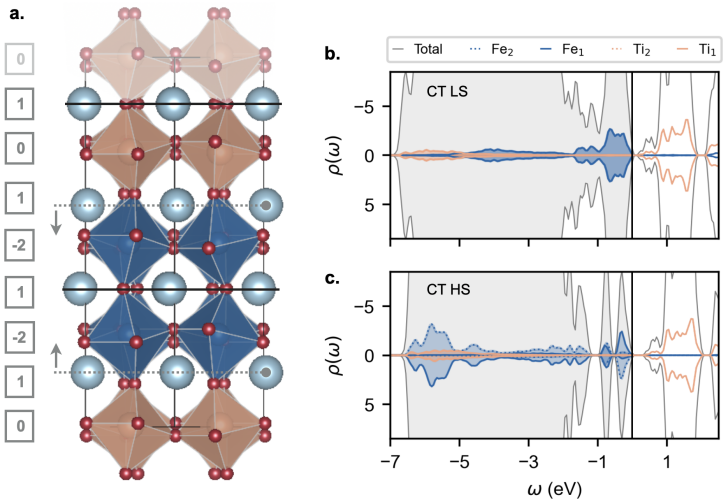

Figure S11: **a.** $(LaTiO3)_2/(LaFeO3)_2$ heterostructure with charge transfer from Ti to Fe. The panel includes also the nominal charge in each layer and the alignment or displacement of the La ions from the oxygen plane toward the FeO_2 layers (as indicated by the arrows). Density of states obtained for the configurations with charge transfer and Fe^{2+} being respectively in **b.** low spin (CT LS) and **c.** high spin (CT HS). The full Ti-d and Fe-d manifolds are shown and are decomposed into their $Fe_{1,2}$ or $Ti_{1,2}$ spatial labels.